

# Sequential Neural Operator Transformer for High-Fidelity Surrogates of Time-Dependent Non-linear Partial Differential Equations

Qibang Liu<sup>a,c,\*</sup>, Seid Koric<sup>a,b</sup>

<sup>a</sup>National Center for Supercomputing Applications, University of Illinois Urbana-Champaign, Urbana, 61801, IL, USA

<sup>b</sup>The Grainger College of Engineering, Department of Mechanical Science and Engineering, University of Illinois Urbana-Champaign, Urbana, 61801, IL, USA

<sup>c</sup>Department of Industrial and Manufacturing Systems Engineering, Kansas State University, Manhattan, 66506, KS, USA

## ARTICLE INFO

*Keywords:*

Transformer

Sequential Neural Operator

Deep Learning

Attention Mechanism

Surrogate Modeling

## ABSTRACT

Partial differential equations (PDEs) are fundamental to modeling complex and nonlinear physical phenomena, but their numerical solution often requires significant computational resources, particularly when a large number of forward full solution evaluations are necessary, such as in design, optimization, sensitivity analysis, and uncertainty quantification. Recent progress in operator learning has enabled surrogate models that efficiently predict full PDE solution fields; however, these models often struggle with accuracy and robustness when faced with highly nonlinear responses driven by sequential input functions. To address these challenges, we propose the Sequential Neural Operator Transformer (S-NOT), a architecture that combines gated recurrent units (GRUs) with the self-attention mechanism of transformers to address time-dependent, nonlinear PDEs. Unlike S-DeepONet (S-DON), which uses a dot product to merge encoded outputs from the branch and trunk sub-networks, S-NOT leverages attention to better capture intricate dependencies between sequential inputs and spatial query points. We benchmark S-NOT on three challenging datasets from real-world applications with plastic and thermo-viscoplastic highly nonlinear material responses: multiphysics steel solidification, a 3D lug specimen, and a dogbone specimen under temporal and path-dependent loadings. The results show that S-NOT consistently achieves a higher prediction accuracy than S-DON even for data outliers, demonstrating its accuracy and robustness for drastically accelerating computational frameworks in scientific and engineering applications.

## 1. Introduction

Partial differential equations (PDEs) are central to modeling a wide range of physical phenomena, as they encode the governing laws of physics. Traditional numerical methods—such as finite difference, finite element, and finite volume approaches—have been widely used to obtain solutions to these equations. Although these methods can achieve high-fidelity results and capture intricate behaviors, they are often computationally expensive and time-consuming, especially for large-scale or high-dimensional problems. As a result, running such simulations can be prohibitive in terms of both time and computational resources.

Recently, data-driven deep learning approaches—commonly known as surrogate models—have emerged to address these computational challenges across diverse domains, including solid mechanics [1, 2], fluid mechanics, electromagnetics [3, 4], acoustics [5, 6], and chemical polymerization [7, 8], among others. Leveraging neural networks, these methods can efficiently approximate PDE solutions, enabling substantial reductions in computational cost and accelerating simulations while maintaining high accuracy. Such surrogate models are particularly beneficial for tasks that require repeated PDE evaluations, such as uncertainty quantification [9, 10], sensitivity analysis [11, 12], and optimization using gradient-based methods [13, 14] or generative AI designs [15, 16].

DeepONet [17] is a widely used surrogate model that employs artificial neural networks to approximate nonlinear operators mapping input functions to outputs at specified query points:

$$G_\theta : \mathcal{F} \rightarrow \mathcal{G}(\mathbf{x}), \quad (1)$$

*Email address:* qibang@illinois.edu (Q. Liu)

where  $G_\theta$  denotes the neural operator parameterized by  $\theta$ ,  $\mathcal{F}$  is the space of input functions, and  $\mathcal{S}$  is the space of output functions evaluated at query points  $\mathbf{x}$ .

The original DeepONet framework [17] consists of two fully connected neural networks (FNNs): a branch network that encodes the input function at specified sensor locations, and a trunk network that encodes the spatiotemporal coordinates of the solution. The outputs of these networks are combined via a dot product to predict the solution, which is then compared to reference values from conventional numerical methods. DeepONet has been successfully applied to predict full-field solutions in a range of fields, including materially nonlinear solid mechanics [18], fracture mechanics [19], aerodynamics [20], acoustics [21], seismology [22], digital twins [23], heat transfer [24, 25], and real-time monitoring [26], among others. However, these applications typically focus on static or stationary loads, and do not address time-dependent loading scenarios. In practice, many real-world loads—such as wind, vibration, or impact—are inherently time-dependent. A standard FNN in the branch network is not designed to preserve the causality present in sequential input data. To overcome this limitation, He et al. [27] proposed the Sequential DeepONet (S-DON), which replaces the FNN in the branch network with gated recurrent units (GRUs) to better capture the sequential characteristics of time-dependent inputs.

While S-DON has demonstrated notably improved performance for time and path-dependent problems compared the original DeepONet, its reliance on a simple dot product to merge branch and trunk outputs can limit its ability to capture complex dependencies, especially across all challenging scenarios. Recent advances have introduced the use of transformer-based attention mechanisms [28] in neural operators, leading to the development of Neural Operator Transformers (NOT) [16, 29–33]. Moreover, the recent work by Shih et al. [34] established a theoretical groundwork that a transformer with cross-attention possesses the universal approximation property as an operator learning model. Unlike the simple dot product, the attention mechanism enables each query point to selectively aggregate information from the input functions, allowing the model to better capture intricate relationships and dependencies. Moreover, since transformers were originally designed to model long-range dependencies in sequential data, they are particularly well-suited for learning the complex spatiotemporal interactions present in PDE solutions under time and path-dependent loading.

In this work, we introduce the Sequential Neural Operator Transformer (S-NOT), a novel framework for solving time and path-dependent nonlinear problems with improved accuracy and generalization. S-NOT combines the sequential modeling capabilities of gated recurrent units (GRUs) with the self-attention and cross-attention mechanisms of transformer architectures to effectively encode sequential loading data and predict solution fields at query points. We evaluate S-NOT on three representative datasets: multiphysics steel solidification, a 3D lug specimen, and a dog-bone specimen under time-dependent loading. Comparative results demonstrate that S-NOT consistently achieves higher prediction accuracy than S-DON across all test cases.

This manuscript presents the Sequential Neural Operator Transformer (S-NOT) framework, detailing its architecture, methodology, and performance. Section 2 outlines the S-DON and S-NOT models, while Section 3 introduces the three benchmark datasets used for training and evaluation. The main results are discussed in Section 4, and key findings are summarized in Section 5.

## 2. Methodology

### 2.1. Sequential DeepONet

The original DeepONet framework [17] has two fully connected neural networks (FNNs): the branch network, which encodes the input function at designated sensor locations, and the trunk network, which encodes the spatiotemporal coordinates of the solution. DeepONet integrates the outputs of these two networks via a dot product to forecast the solution, which is subsequently compared with target values generated from conventional numerical approaches. The prediction error is measured via a loss function, whose gradients with respect to the trainable parameters of neural networks are calculated during backpropagation, allowing the optimizer to repeatedly enhance the weights and biases in both networks. With adequate training epochs—iterations of feedforward and backpropagation—DeepONet acquires the ability to forecast the whole solution field throughout the domain.

In cases characterized by irreversible material deformation or thermo-mechanical multiphysics, where plastic or thermo-viscoplastic behavior creates path or time dependency, the complete load history is essential for precisely ascertaining the final stress state. The Sequential DeepONet (S-DON) [27] was recently introduced to enhance the management of sequential input functions in these scenarios. This architecture substitutes the conventional feedforward neural network in the branch network with an encoder-decoder model utilizing gated recurrent units (GRUs), better at

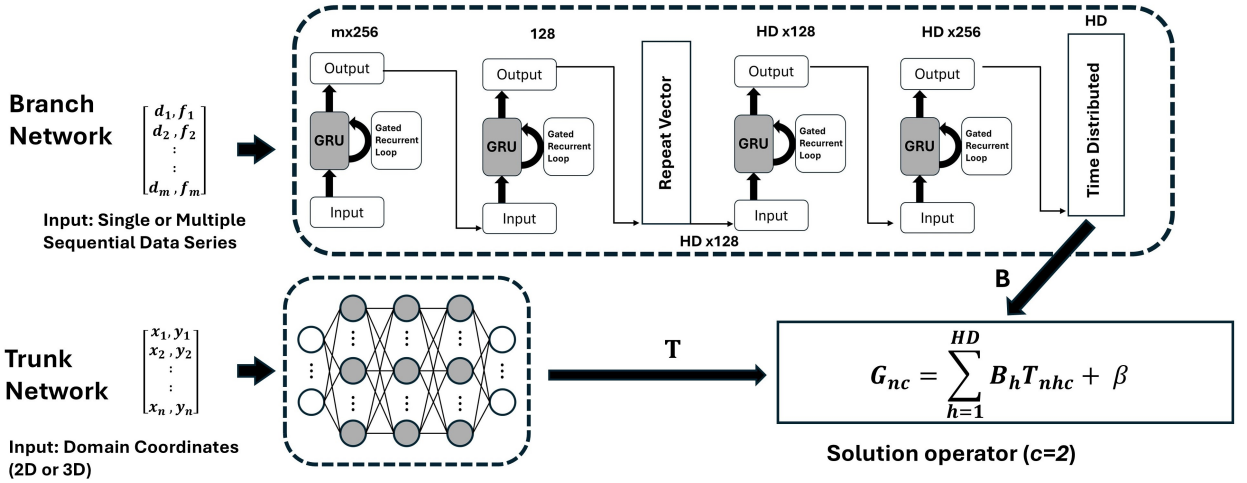


Fig. 1: S-DON architecture.

capturing the sequence of the input data. Gating methods in GRUs address vanishing gradient issues and facilitate the learning of long-term dependencies, rendering them more effective for sequential learning than conventional recurrent neural networks. Although the training duration was extended compared to the original DeepONet, the S-DON model substantially enhanced predictive accuracy [27] and became the standard in sequential operator learning. Fig. 1 illustrates the architecture with a single branch that encodes single or multiple sequential inputs (such as  $d_i$  and  $f_i$ ) in a coupled fashion via a series of encoder-decoder GRU cells, yielding an encoded branch output  $B_h$  with hidden dimension. The trunk network encodes  $n$  input domain 2D or 3D coordinates into its multidimensional output  $T_{nhc}$ , where  $c$  denotes the number of output solution fields predicted concurrently, such as temperature and stress, or plastic strain and stress in the examples in this work. The encoded outputs from the branch and trunk are combined by a dot product to get the final S-DON prediction  $G_{nc}$ , incorporating a bias  $\beta$  along the hidden dimension. For a more detailed description of the S-DON architecture and its applications, one can consult [27, 35].

## 2.2. Sequential Neural Operator Transformer (S-NOT)

S-NOT combines the transformer architecture with the neural operator framework to predict solution fields at query nodes under varying sequential loading. The model consists of two main components: a sequential loading encoder and a solution decoder, as shown in Fig. 2. Both components utilize the attention mechanism from the transformer architecture [28], enabling the model to selectively focus on relevant input features. The attention operation is defined as

$$\text{Attention}(Q, K, V) = \text{softmax}\left(\frac{QK^T}{\sqrt{d_e}}\right)V, \quad (2)$$

where  $Q \in \mathbb{R}^{N_q \times d_e}$  is the QUERY matrix, and  $K, V \in \mathbb{R}^{N_k \times d_e}$  are the KEY and VALUE matrices, respectively. Here,  $d_e$  is the embedding dimension,  $N_q$  is the number of query points, and  $N_k$  is the length of the KEY and VALUE sequences. Each attention block incorporates residual connections and layer normalization to promote stable training, as illustrated in the lower right of Fig. 2.

The encoder processes the sequential loading data using a stack of GRUs, as in S-DON, to capture temporal dependencies. The GRU outputs are augmented with sinusoidal positional encodings [28] to incorporate time information explicitly. This enriched representation, containing both loading values and temporal context, is projected via a linear layer to form the QUERY, KEY, and VALUE matrices for multiple self-attention blocks. The self-attention blocks enable the model to further selectively focus on the most informative aspects of the sequential input functions, improving S-NOT's ability to capture the underlying relationships between the elements in input space. The encoder's final output, shaped as  $N_k \times d_e$ , serves as the KEY and VALUE inputs to the decoder's cross-attention layers.

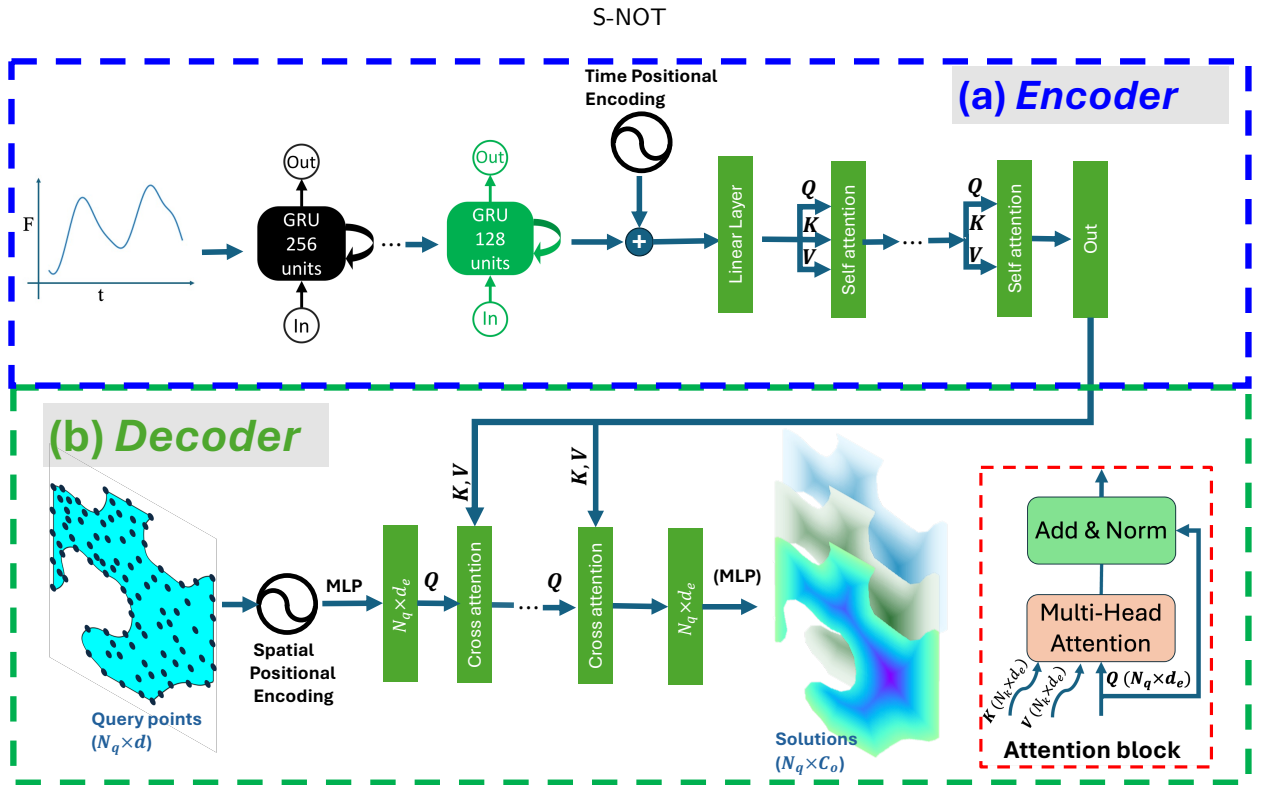


Fig. 2: Overview of the S-NOT architecture.

The solution decoder generates predictions at the query points by leveraging the sequential representations from the encoder. Each query point is first embedded using a NeRF-style positional encoding [36], followed by a multilayer perceptron (MLP), to produce the QUERY matrix of size  $N_q \times d_e$ , where  $N_q$  is the number of query points and  $d_e$  is the embedding dimension. This QUERY is then combined with the encoder's KEY and VALUE outputs through cross-attention blocks, replacing the fixed inner product used in S-DON. This approach enables each query point to selectively aggregate relevant information from the sequential loading history, thereby enhancing the model's capacity to capture complex dependencies and supporting the universal approximation property in operator learning. The resulting representations of cross-attention are passed through a final MLP to produce the predicted solution fields at the query locations. The overall structure of the solution decoder is depicted in Fig. 2(b).

### 3. Example datasets

In this section, we introduce the three benchmark datasets used to train and evaluate the S-NOT model. The first dataset involves a multiphysics steel solidification problem with time-dependent heat flux and displacement boundary conditions. The second dataset features a 3D lug specimen subjected to time-varying pressure loading. The third dataset consists of a dog-bone specimen under sequential displacement loading. These datasets represent a range of challenging, time-dependent physical scenarios for assessing the performance and generalization of the proposed model.

#### 3.1. Multiphysics Steel Solidification

To generate training and validation datasets for our operator learning frameworks, in the first example, we use a real-world multiphysics (thermo-mechanical) finite element simulation that numerically models the solidification of a 2D slice in a continuous steel caster. Over 95% of steel worldwide is produced nowadays by the continuous casting process, which makes this example extremely relevant. The solidifying slice is modeled in a Lagrangian reference frame, tracking its evolution through the mold region. The thermal evolution is governed by an energy conservation equation in Eq. (3) that incorporates material density ( $\rho$ ), temperature-dependent conductivity ( $k$ ), and enthalpy ( $H$ ),

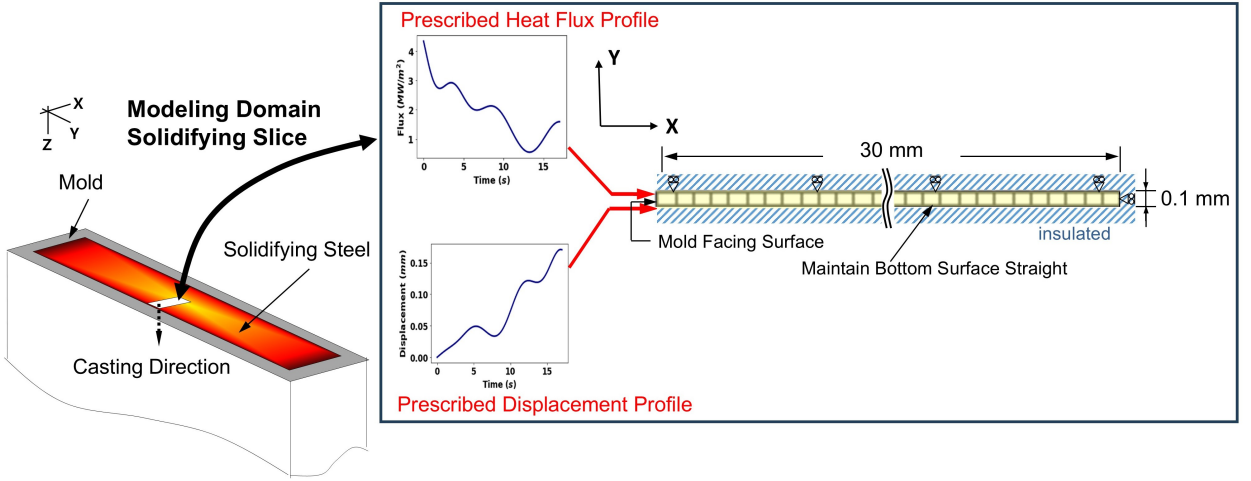


Fig. 3: 'Slice modeling domain in caster with boundary value conditions.

which accounts for latent heat due to solid-state transformations such as  $\delta$ -ferrite to austenite transitions.

$$\rho \frac{\partial H}{\partial t} = \nabla \cdot (k \nabla T) \quad (3)$$

Given the negligible influence of inertia during solidification, mechanical equilibrium is treated as quasi-static in Eq. (4):

$$\nabla \cdot \boldsymbol{\sigma}(\mathbf{x}) + \mathbf{b} = 0 \quad (4)$$

Here,  $\boldsymbol{\sigma}$  is the Cauchy stress tensor, and  $\mathbf{b}$  is the body force density. The stress equilibrium is solved concurrently with the thermal field, with mechanical behavior captured using a thermo-elastic-viscoplastic formulation. The total strain rate tensor  $\dot{\boldsymbol{\epsilon}}$  is decomposed into elastic, inelastic, and thermal contributions;  $\dot{\boldsymbol{\epsilon}}_{el}$ ,  $\dot{\boldsymbol{\epsilon}}_{ie}$ ,  $\dot{\boldsymbol{\epsilon}}_{th}$  in Eq. (5).

$$\dot{\boldsymbol{\epsilon}} = \dot{\boldsymbol{\epsilon}}_{el} + \dot{\boldsymbol{\epsilon}}_{ie} + \dot{\boldsymbol{\epsilon}}_{th} \quad (5)$$

The thermal strain depends on the temperature distribution and the temperature-dependent thermal expansion coefficient,  $\alpha$ . Stress and strain rates are related in Eq. (6)

$$\boldsymbol{\sigma} = \mathbf{D} : (\dot{\boldsymbol{\epsilon}} - \alpha \mathbf{I} \dot{T} - \dot{\boldsymbol{\epsilon}}_{ie}) \quad (6)$$

In this equation,  $\mathbf{D}$  is a fourth-order tensor that contains the temperature-dependent elastic constants for an isotropic material, and  $\mathbf{I}$  is the identity tensor.

The mechanical response of solidifying steel is highly nonlinear, exhibiting time- and temperature-dependent inelastic deformation. For the austenite phase, we use a viscoplastic model originally proposed by Kozłowski et al. [37], which relates the equivalent inelastic strain rate  $\dot{\bar{\boldsymbol{\epsilon}}}_{ie}$  ie to Von Mises stress  $\bar{\sigma}$  (MPa), absolute temperature, and steel grade determined by carbon content %C given in Eq. (5)

$$\dot{\bar{\boldsymbol{\epsilon}}}_{ie} [\text{sec}^{-1}] = f_C \left( \bar{\sigma} [\text{MPa}] - f_1 \bar{\boldsymbol{\epsilon}}_{ie} |\bar{\boldsymbol{\epsilon}}_{ie}|^{f_2-1} \right)^{f_3} \exp \left( -\frac{Q}{T [\text{K}]} \right) \quad (7)$$

where

$$\begin{aligned} Q &= 44.465 \\ f_1 &= 130.5 - 5.128 \times 10^{-3} T [\text{K}] \\ f_2 &= -0.6289 + 1.114 \times 10^{-3} T [\text{K}] \\ f_3 &= 8.132 - 1.54 \times 10^{-3} T [\text{K}] \\ f_c &= 46,550 + 71,400(\%C) + 12,000(\%C)^2 \end{aligned} \quad (8)$$

$Q$  is an activation energy constant, and the empirical functions  $f_1, f_2, f_3, f_c$  vary with absolute temperature and carbon content.

In contrast,  $\delta$ -ferrite phase, characterized by lower strength and greater creep susceptibility, is described using the Zhu power law model [38]. When the  $\delta$ -ferrite phase exceeds 10% of the local microstructure, this model governs the material response. In mushy zones above the solidus temperature, we assume a nearly negligible yield stress using an elastic-perfectly-plastic model.

These constitutive equations are implemented and locally integrated within a user-defined material subroutine (UMAT) in the Abaqus implicit finite element analysis code [39]. The UMAT computes phase fractions and interpolates material properties as functions of temperature for a selected low-carbon steel (0.09 wt% C), with solidus and liquidus temperatures of 1480.0 °C and 1520.7 °C, respectively. More detailed descriptions of this robust multiphysics model are provided in [40, 41].

The computational domain traveling down the caster, depicted in Fig. 3, is a 2D slice subjected to generalized plane strain assumptions in the axial direction to emulate 3D stress states relevant to long and wide caster geometries. The domain consists of 300 coupled thermo-mechanical quadrilateral elements and 602 nodes. A fixed bottom boundary condition ensures uniform vertical strain, while thermal and displacement profiles are applied on the left boundary to simulate interaction with the mold.

Transient boundary conditions are imposed to reflect the casting process: heat fluxes evolve over time due to changing contact conditions, and the displacements reflect mold taper effects. These profiles are based on plant measurements and are perturbed using Gaussian radial basis interpolation to mimic realistic noise and variability observed in operating conditions. This ensures that the generated data captures a broad spectrum of physical scenarios encountered during casting. More details about these thermal and mechanical input sequences can be found at [42], where they were used for non-operator deep learning.

5000 data samples were generated utilizing the high-throughput and parallel CPU processing capabilities of the Delta high-performance cluster at the National Center for Supercomputing Applications (NCSA) [43]. Each data sample consists of input sequences, and the final lateral stress and temperature solutions at the mold exit are used as labels. They were used to train the Sequential DeepONet (S-DON) and the Sequential Neural Operator Transformer (S-NOT) models. The complete dataset was divided, with 80% allocated for training and the remaining 20% allocated for testing. Computational nodes equipped with Nvidia H200 GPUs in the DeltaAI [44] cluster were used to train both S-DON and S-NOT models.

### 3.2. 3D-LUG

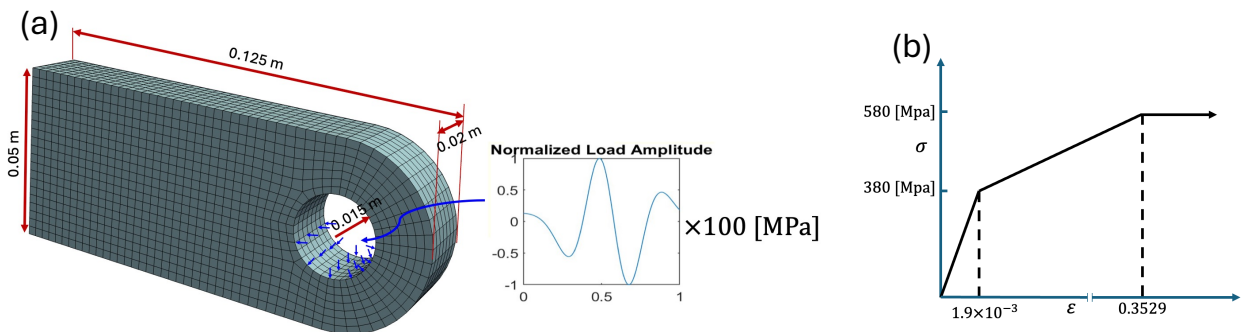


**Fig. 4:** The 3D LUG specimen for FEM simulation. (a) The lug geometry, FE mesh, and time-dependent loading profile. (b) the material properties used in the simulation.

In the second example, we consider a 3D lug specimen subjected to time-dependent pressure loading. The geometry, finite element mesh, and loading profile are shown in Fig. 4(a). Lugs are widely used structural components, and accurately predicting their mechanical response is important for assessing system performance and reliability. In this setup, a random time-dependent normal pressure is applied to the bottom half of the circular hole.

The lug is discretized using 6,336 second-order hexahedral elements, resulting in 29,852 nodes. The material behavior is modeled with an elastic-plastic constitutive law with linear isotropic hardening:

$$\sigma_y(\epsilon_p) = \sigma_{pe} + H\epsilon_p \quad (9)$$

where  $\sigma_y$  is the flow stress,  $\epsilon_p$  is the equivalent plastic strain,  $\sigma_{pe}$  is the initial yield stress, and  $H$  is the hardening modulus. The specific material properties used are summarized in Fig. 4(b).

To generate the dataset, random loading profiles are sampled from a Gaussian random field. A total of 10,000 paired samples of loading profiles, the final state of von Mises stress, and plastic equivalent strain (PEEQ) are generated. The dataset is split into 80% for training and 20% for testing.

### 3.3. Dog-bone

The third example involves a dog-bone specimen subjected to sequential, time-dependent displacement loading, as illustrated in Fig. 5. This dataset, originally introduced by He et al. [27], features the specimen fixed on the left boundary, while the right boundary experiences a randomly generated displacement sequence over time, following the same protocol as the previous cases. The mechanical behavior is described by an elastic-plastic constitutive model with linear isotropic hardening. Comprehensive details regarding the material parameters, finite element modeling, and data generation can be found in He et al. [27]. The dataset comprises 15,000 samples, each containing a loading profile, the final state of von Mises stress, and plastic equivalent strain (PEEQ). For model evaluation, 3,200 samples are used for training and 800 for testing to assess the generalization performance of S-NOT.

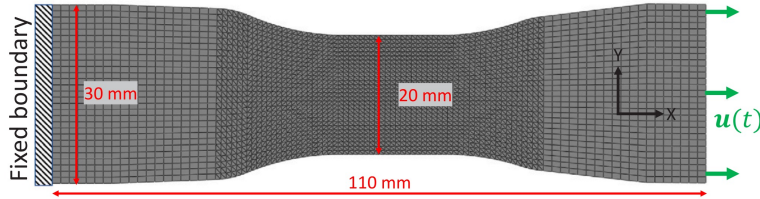


Fig. 5: The dog bone specimen.

## 4. Results

In this section, we present the prediction results for the three benchmark datasets introduced in Section 3. To evaluate model performance, we use the relative  $L_2$  error for stress predictions, defined as

$$L^2 = \frac{1}{N_P} \sum_{i=1}^{N_P} \frac{\|\mathbf{S}_i^{\text{true}} - \mathbf{S}_i^{\text{predict}}\|_2}{\|\mathbf{S}_i^{\text{true}}\|_2} \quad (10)$$

where  $\mathbf{S}_i^{\text{true}}$  and  $\mathbf{S}_i^{\text{predict}}$  denote the true and predicted full-field solutions for the  $i$ -th test sample, and  $\|\cdot\|_2$  is the Euclidean norm.

For the PEEQ predictions, we use the mean absolute error (MAE) as the evaluation metric, defined as

$$\text{MAE} = \frac{1}{N_P} \sum_{i=1}^{N_P} |\mathbf{S}_i^{\text{true}} - \mathbf{S}_i^{\text{predict}}| \quad (11)$$

The performance of S-NOT is compared against S-DON, with a summary provided in Table 1 and detailed results discussed in the following subsections.

Table 2 compares the computational efficiency and model size of S-NOT and S-DON. S-NOT offers similar inference speed and parameter count to S-DON, while delivering improved prediction accuracy.

**Table 1**

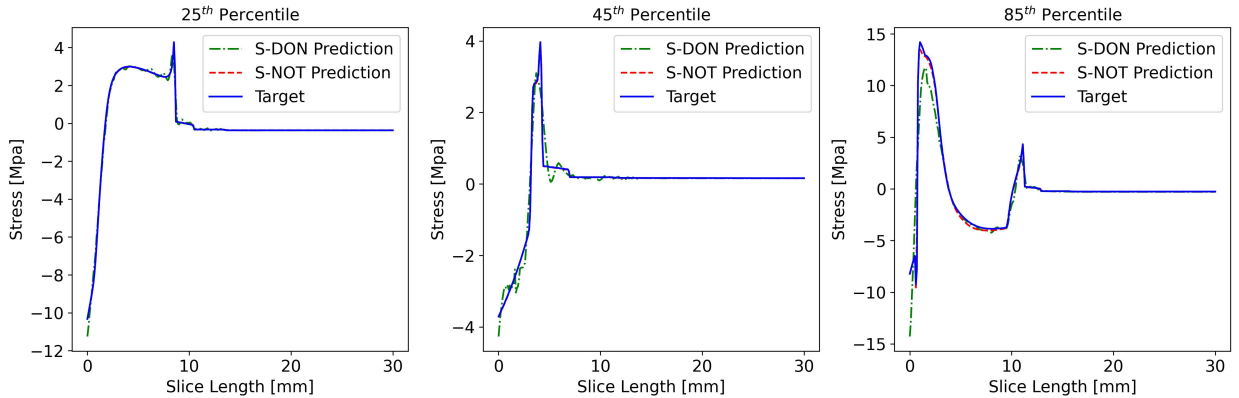
Comparison of S-NOT and S-DON performance on the three benchmark datasets. Reported values are mean errors over all test samples, with standard deviation in parentheses. '-' indicates unavailable data.

Method	Stress $L_2$ error [%]		PEEQ MAE [ $\times 10^{-4}$ ]		Temperature $L_2$ error [%]	
	S-DON	S-NOT	S-DON	S-NOT	S-DON	S-NOT
Steel Solidification	18.1 (23.2)	4.3 (15.3)	-	-	0.091 (0.49)	0.04 (0.52)
3D Lug	11.6 (36.5)	5.31 (15.1)	1.4 (4.74)	0.76 (3.67)	-	-
Dog-bone	2.01 (6.19)	1.13 (3.59)	0.79 (2.37)	0.27 (1.5)	-	-

**Table 2**

Comparison of computational efficiency and model size for S-NOT, S-DON, and FEM across the three benchmark problems. Reported are the number of trainable parameters and average inference time per sample (GPU), alongside reference FEM simulation time (CPU).

Method	Number of param		Inference time (GPU) [s/sample]		FEM simulation (CPU) [s/sample]
	S-DON	S-NOT	S-DON	S-NOT	
Steel Solidification	772,674	805,592	7.33e-4	1.1e-3	333
3D Lug	2,007,426	1,138,689	4.7e-3	2.87e-3	80
Dog-bone	771,906	7,90952	9e-4	1.2e-3	20

**Fig. 6:** Stress Comparison, Multiphysics Solidification.

#### 4.1. Multiphysics Steel Solidification

Both S-DON and S-NOT accurately predict the temperature distributions, which are relatively smooth, as indicated by the low mean relative  $L_2$  norm error across all test samples (Eq. (10)). In contrast, stress distributions are more challenging due to the influence of three constitutive models (austenite, delta-ferrite, and mushy/liquid), temperature-dependent thermal stresses, and the complex, time-varying displacement history applied to the cooled surface. These factors lead to highly irregular lateral stress profiles throughout the slice domain, making precise prediction difficult. S-NOT achieves substantially higher accuracy, with a mean stress  $L_2$  error of **4.3%**, compared to **18.1%** for S-DON, and a mean temperature  $L_2$  error of **0.04%** versus **0.091%** for S-DON, as shown in Table 1.

Fig. 6 shows predicted and reference stress values at the mold exit along the slice domain for test samples at the 25th, 45th, and 85th percentiles (ranked by  $L_2$  error). The difference between models is especially pronounced in the 85th percentile sample, where S-DON deviates significantly from both the target and S-NOT predictions, particularly at the chilled surface (0 mm) and within the solid phase. Accurate prediction of lateral stress at the chilled surfaces is critical for forecasting failure mechanisms in steel casting, such as hot tearing, highlighting the importance of S-NOT's improved performance.

The test error histograms for both temperature and stress in Fig. 7 further illustrate the superior accuracy of S-NOT over S-DON, where S-DON exhibits a longer tail of higher error values.

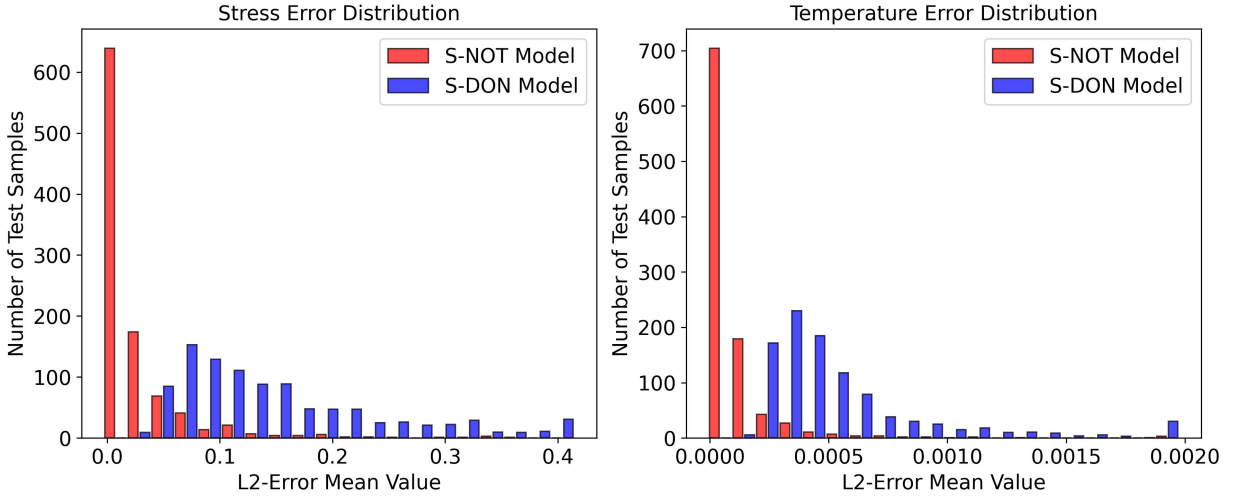


Fig. 7: Test L2 errors Distribution (histograms) of the Multiphysics Slice.

## 4.2. 3D-LUG

For the 3D-LUG example, model accuracy is evaluated using the relative  $L_2$  error for stress and the mean absolute error (MAE) for PEEQ. S-NOT achieves a relative  $L_2$  error of 5.31% for stress, outperforming S-DON's 11.6%. For PEEQ, S-NOT attains an MAE of  $7.62 \times 10^{-5}$ , which is notably lower than S-DON's  $1.4 \times 10^{-4}$ .

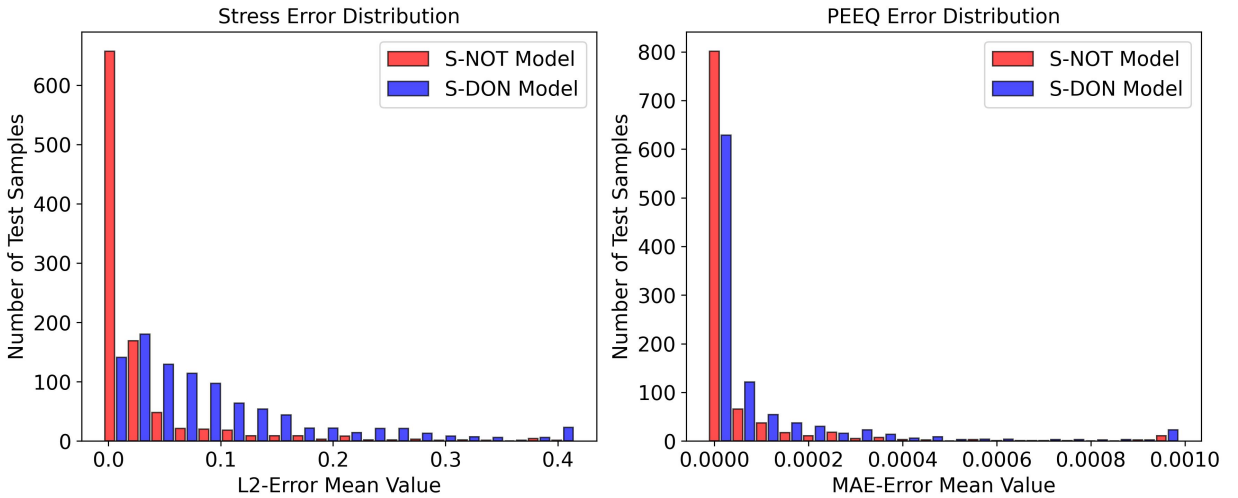
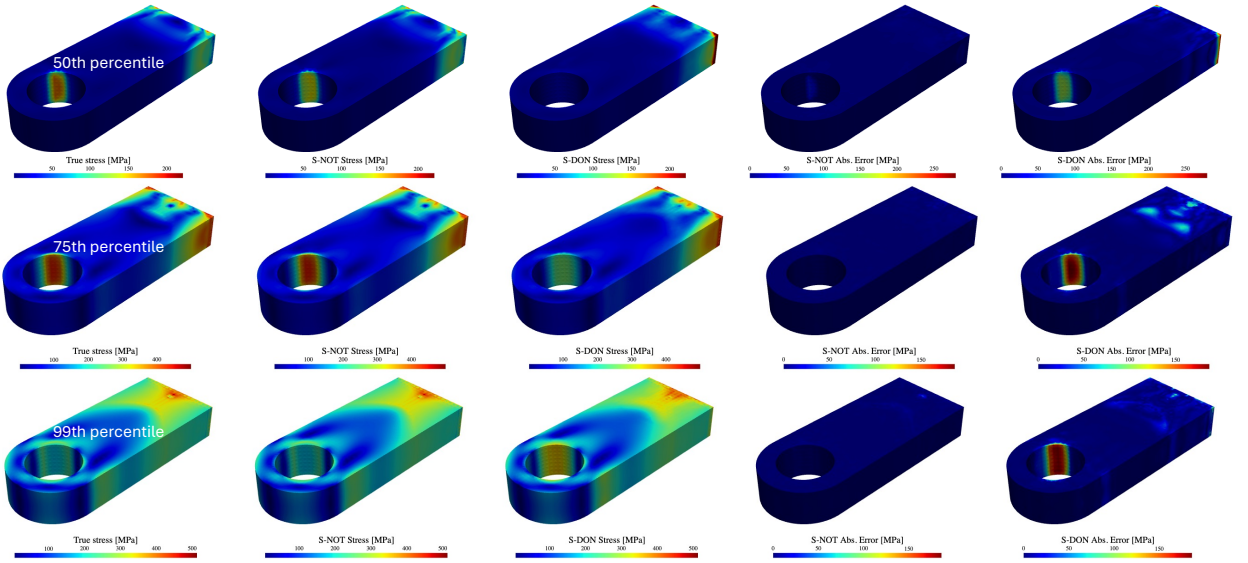


Fig. 8: test L2 errors Distribution (histograms) of the 3D LUG.

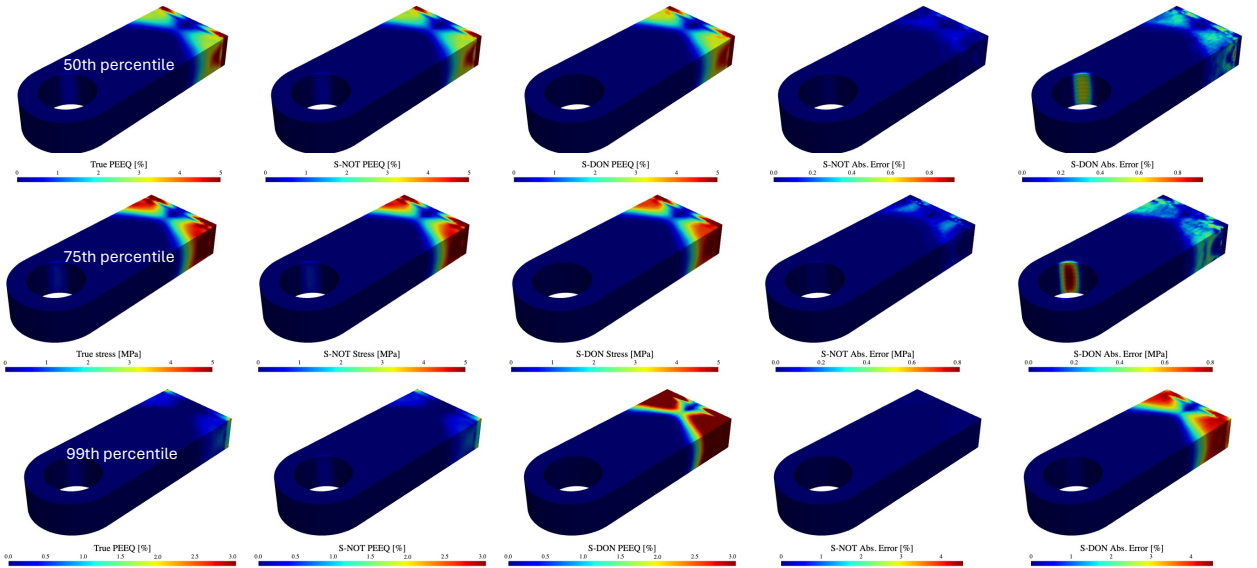
The histograms of test error distributions for both PEEQ and stress in Fig. 8 highlight the superior accuracy of S-NOT compared to S-DON, particularly for stress predictions, where S-DON exhibits a longer tail of higher error values (blue columns), and less samples with high accuracy compared to S-NOT (red columns).

Fig. 9 presents a comparison of predicted and reference stress values for test samples at the 50th, 75th, and 99th percentiles (by relative  $L_2$  error). The difference between the models is especially pronounced in these cases, with S-DON deviating significantly from the target in the hole region, while S-NOT predictions remain much closer to the reference across the entire domain. A similar trend is observed for PEEQ in Fig. 10, where S-NOT consistently achieves lower absolute errors than S-DON.

## S-NOT



**Fig. 9:** Stress comparison for the 3D LUG example: True vs S-NOT vs S-DON. Each row corresponds to a test sample at the 50th, 75th, and 99th percentiles (by relative  $L_2$  error). Columns show: (1) true stress, (2) S-NOT prediction, (3) S-DON prediction, (4) error between S-NOT and true, and (5) error between S-DON and true.



**Fig. 10:** PEEQ comparison for the 3D LUG example: True vs S-NOT vs S-DON. Rows correspond to the 50th, 75th, and 99th percentile test samples (by relative  $L_2$  error). Columns show: (1) true PEEQ, (2) S-NOT prediction, (3) S-DON prediction, (4) error between S-NOT and true, and (5) error between S-DON and true.

### 4.3. Dog-bone

For the dog-bone example, model performance is evaluated using the relative  $L_2$  error for stress and the mean absolute error (MAE) for PEEQ. S-NOT achieves a relative  $L_2$  error of 1.13% for stress, outperforming S-DON's 2.01%. For PEEQ, S-NOT attains an MAE of  $2.67 \times 10^{-5}$ , which is notably lower than S-DON's  $7.85 \times 10^{-5}$ .

The histogram of test error distributions for both PEEQ and stress in Fig. 11 highlights the improved accuracy of S-NOT over S-DON, particularly for PEEQ predictions, where the majority of S-NOT results (red columns) outperform even the best S-DON predictions (blue columns).

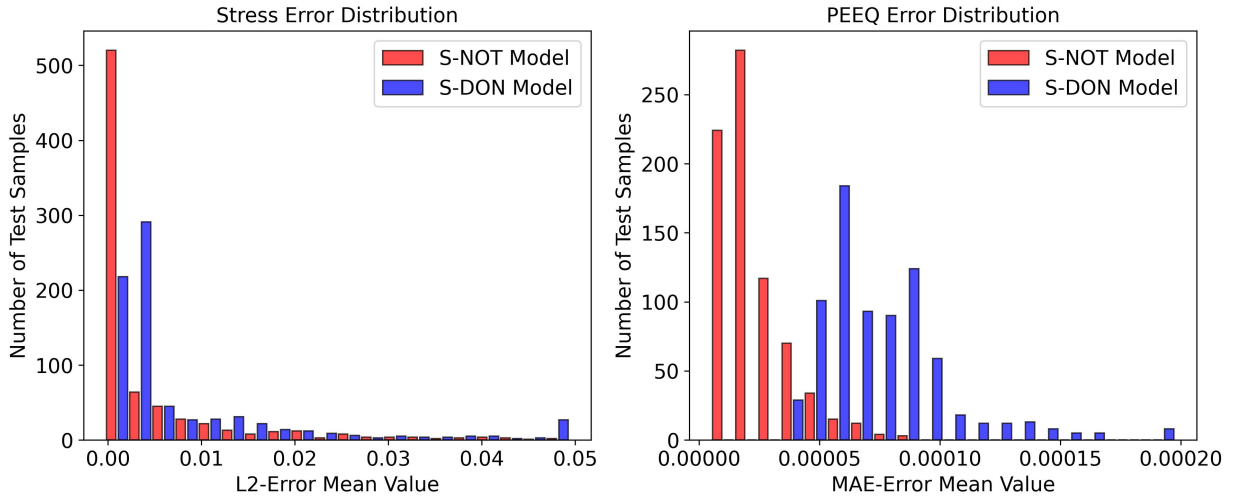


Fig. 11: test  $L_2$  errors Distribution (histograms) of the Dog-bone.

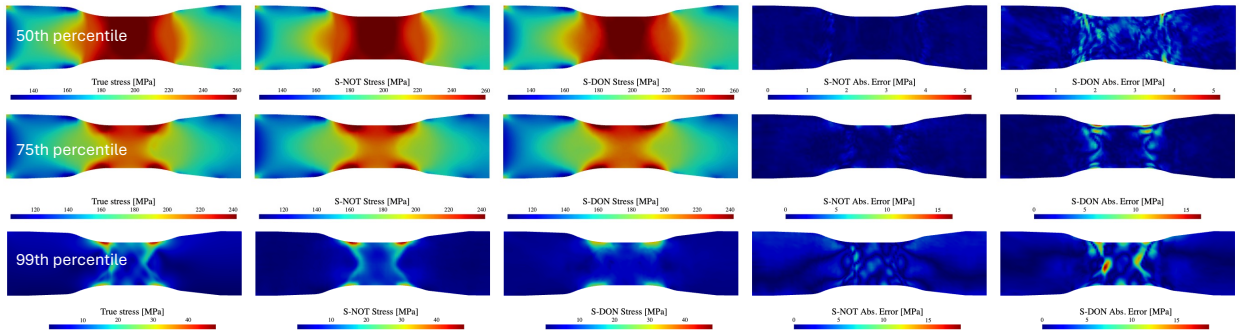


Fig. 12: Stress comparison for the dog-bone example: True vs S-NOT vs S-DON. Rows correspond to the 50th, 75th, and 99th percentile test samples (by relative  $L_2$  error). Columns show: (1) true stress, (2) S-NOT prediction, (3) S-DON prediction, (4) error between S-NOT and true, and (5) error between S-DON and true.

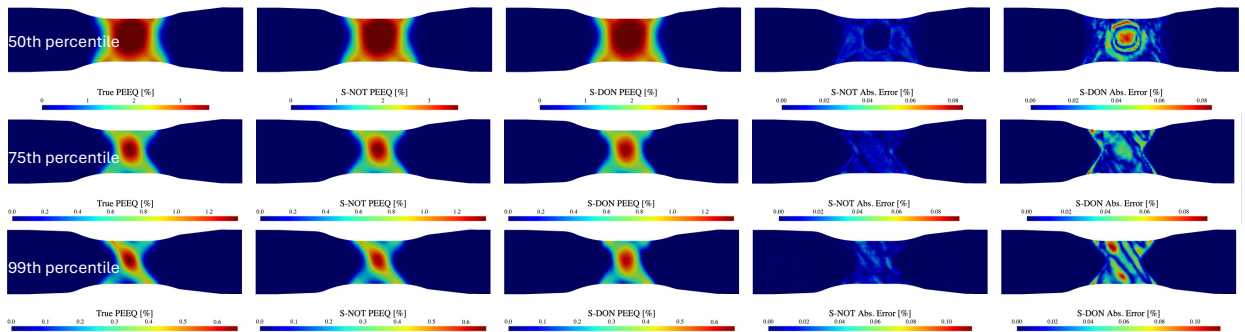


Fig. 13: PEEQ comparison for the dog-bone example: True vs S-NOT vs S-DON. Rows correspond to the 50th, 75th, and 99th percentile test samples (by relative  $L_2$  error). Columns show: (1) true PEEQ, (2) S-NOT prediction, (3) S-DON prediction, (4) error between S-NOT and true, and (5) error between S-DON and true.

Fig. 12 presents a comparison of predicted and reference stress values for test samples at the 50th, 75th, and 99th percentiles (by relative  $L_2$  error). The difference between the models is especially pronounced in these cases, with

S-DON deviating significantly from the target in the critical regions, while S-NOT predictions remain much closer to the reference across the entire domain. A similar trend is observed for PEEQ in Fig. 13, where S-NOT consistently achieves lower absolute errors than S-DON.

## 5. Conclusions

In this work, we presented the Sequential Neural Operator Transformer (S-NOT), a novel deep learning framework for efficiently solving time and path-dependent nonlinear partial differential equations (PDEs). By combining gated recurrent units (GRUs) for sequential encoding with transformer-based attention mechanisms, S-NOT captures complex temporal and spatial dependencies in physical systems. The use of cross-attention enables the model to selectively aggregate relevant information for each query point, addressing the limitations of dot product-based approaches such as Sequential DeepONet (S-DON).

Benchmarking S-NOT on three highly nonlinear datasets originating from real-world simulations of multiphysics steel solidification, a 3D lug specimen, and a dog-bone specimen under sequential loadings, consistently demonstrated improved prediction accuracy and generalization compared to S-DON, particularly among outlier test samples with a higher than 90th percentile error, where S-DeepONet's accuracy regularly dropped. These results indicate that S-NOT is a robust and an effective surrogate model for enabling scientific and engineering workflows that require frequent, rapid, and accurate full-field solutions of time and path-dependent PDEs, including uncertainty quantification and sensitivity analysis, optimizations, inverse designs, online controls, and digital twins.

## 6. Data availability

The dataset is available on Zenodo and the trained models are available at the GitHub repository <https://github.com/QibangLiu/SNOT>

## 7. Code availability

The codes for training and inference are available at the GitHub repository at <https://github.com/QibangLiu/SNOT>

## 8. Acknowledgements

The authors would like to thank the National Center for Supercomputing Applications (NCSA) at the University of Illinois, and particularly its Research Computing Directorate, Industry Program, and Center for Artificial Intelligence Innovation (CAII) for support and hardware resources. This research used both the DeltaAI advanced computing and data resource, which is supported by the National Science Foundation (award OAC 2320345) and the State of Illinois, and the Delta advanced computing and data resource which is supported by the National Science Foundation (award OAC 2005572) and the State of Illinois. Delta and DeltaAI are joint efforts of the University of Illinois Urbana-Champaign and its National Center for Supercomputing Applications.

## 9. Author contributions statement

**Q. Liu** and **S. Koric** jointly conceptualized the study, designed the methodology, implemented the models, performed the analyses, and contributed to writing, reviewing, and editing the manuscript. **S. Koric** was responsible for dataset preparation.

## 10. Competing interests statement

The authors declare no competing financial or non-financial interests.

## References

- [1] S. Kiranyaz, J. Malik, H. B. Abdallah, T. Ince, A. Iosifidis, M. Gabbouj, Exploiting heterogeneity in operational neural networks by synaptic plasticity, *Neural Computing and Applications* 33 (2021) 7997–8015. doi:10.1007/s00521-020-05543-w.

- [2] Z. Yang, C.-H. Yu, M. J. Buehler, Deep learning model to predict complex stress and strain fields in hierarchical composites, *Science Advances* 7 (2021) eabd7416. doi:10.1126/sciadv.abd7416.
- [3] H. Sun, L. Peng, S. Huang, S. Li, Y. Long, S. Wang, W. Zhao, Development of a physics-informed doubly fed cross-residual deep neural network for high-precision magnetic flux leakage defect size estimation, *IEEE Transactions on Industrial Informatics* 18 (2021) 1629–1640. doi:10.1109/TII.2021.3089333.
- [4] Z. Peng, B. Yang, Y. Xu, F. Wang, L. Liu, Y. Zhang, Rapid surrogate modeling of electromagnetic data in frequency domain using neural operator, *IEEE Transactions on Geoscience and Remote Sensing* 60 (2022) 1–12. doi:10.1109/TGRS.2022.3222507.
- [5] T. Konuk, J. Shragge, Physics-guided deep learning using fourier neural operators for solving the acoustic vti wave equation, in: 82nd EAGE annual conference & exhibition, volume 2021, European Association of Geoscientists & Engineers, 2021, pp. 1–5. doi:10.3997/2214-4609.202113304.
- [6] N. Borrel-Jensen, S. Goswami, A. P. Engsig-Karup, G. E. Karniadakis, C.-H. Jeong, Sound propagation in realistic interactive 3d scenes with parameterized sources using deep neural operators, *Proceedings of the National Academy of Sciences* 121 (2024) e2312159120. doi:doi.org/10.1073/pnas.2312159120.
- [7] Q. Liu, D. Abueidda, S. Vyas, Y. Gao, S. Koric, P. H. Geubelle, Adaptive data-driven deep-learning surrogate model for frontal polymerization in dicyclopentadiene, *The Journal of Physical Chemistry B* 128 (2024) 1220–1230. doi:10.1021/acs.jpcc.3c07714.
- [8] P. Cai, S. Liu, Q. Liu, P. H. Geubelle, R. Gomez-Bombarelli, Towards long rollout of neural operators with local attention and flow matching-inspired correction: An example in frontal polymerization PDEs, in: *Machine Learning and the Physical Sciences Workshop @ NeurIPS 2024*, 2024. URL: <https://openreview.net/forum?id=CFNgeuXzPx>.
- [9] M. Abdar, F. Pourpanah, S. Hussain, D. Rezazadegan, L. Liu, M. Ghavamzadeh, P. Fieguth, X. Cao, A. Khosravi, U. R. Acharya, et al., A review of uncertainty quantification in deep learning: Techniques, applications and challenges, *Information fusion* 76 (2021) 243–297. doi:10.1016/j.inffus.2021.05.008.
- [10] S. Cheng, C. Quilodr an-Casas, S. Ouala, A. Farchi, C. Liu, P. Tando, R. Fablet, D. Lucor, B. Iooss, J. Brajard, et al., Machine learning with data assimilation and uncertainty quantification for dynamical systems: a review, *IEEE/CAA Journal of Automatica Sinica* 10 (2023) 1361–1387.
- [11] K. Li, Y. Long, H. Wang, Y.-F. Wang, Modeling and sensitivity analysis of concrete creep with machine learning methods, *Journal of Materials in Civil Engineering* 33 (2021) 04021206. doi:10.1061/(ASCE)MT.1943-5533.0003843.
- [12] S. Wang, Y. Ren, B. Xia, K. Liu, H. Li, Prediction of atmospheric pollutants in urban environment based on coupled deep learning model and sensitivity analysis, *Chemosphere* 331 (2023) 138830. doi:10.1016/j.chemosphere.2023.138830.
- [13] E. M. Dogo, O. Afolabi, N. Nwulu, B. Twala, C. Aigbavboa, A comparative analysis of gradient descent-based optimization algorithms on convolutional neural networks, in: 2018 international conference on computational techniques, electronics and mechanical systems (CTEMS), IEEE, 2018, pp. 92–99. doi:10.1109/CTEMS.2018.8769211.
- [14] M. S. Daoud, M. Shehab, H. M. Al-Mimi, L. Abualigah, R. A. Zitar, M. K. Y. Shambour, Gradient-based optimizer (gbo): a review, theory, variants, and applications, *Archives of Computational Methods in Engineering* 30 (2023) 2431–2449. doi:10.1007/s11831-022-09872-y.
- [15] Q. Liu, P. Cai, D. Abueidda, S. Vyas, S. Koric, R. Gomez-Bombarelli, P. Geubelle, Univariate conditional variational autoencoder for morphogenic pattern design in frontal polymerization-based manufacturing, *Computer Methods in Applied Mechanics and Engineering* 438 (2025) 117848. doi:10.1016/j.cma.2025.117848.
- [16] Q. Liu, S. Koric, D. Abueidda, H. Meidani, P. Geubelle, Towards signed distance function based metamaterial design: Neural operator transformer for forward prediction and diffusion model for inverse design, *arXiv preprint arXiv:2504.01195* (2025). doi:10.48550/arXiv.2504.01195.
- [17] L. Lu, P. Jin, G. Pang, et al., Learning nonlinear operators via deepnet based on the universal approximation theorem of operators, *Nature Machine Intelligence* 3 (2021) 218–229.
- [18] S. Koric, A. Viswanath, D. W. Abueidda, N. A. Sobh, K. Khan, Deep learning operator network for plastic deformation with variable loads and material properties, *Engineering with Computers* 40 (2024) 917–929.
- [19] S. Goswami, M. Yin, Y. Yu, G. E. Karniadakis, A physics-informed variational deepnet for predicting crack path in quasi-brittle materials, *Computer Methods in Applied Mechanics and Engineering* 391 (2022) 114587.
- [20] T. Zhao, W. Qian, J. Lin, H. Chen, H. Ao, G. Chen, L. He, Learning mappings from iced airfoils to aerodynamic coefficients using a deep operator network, *Journal of Aerospace Engineering* 36 (2023) 04023035.
- [21] L. Xu, H. Zhang, M. Zhang, Training a deep operator network as a surrogate solver for two-dimensional parabolic-equation models, *The Journal of the Acoustical Society of America* 154 (2023) 3276–3284.
- [22] E. Haghighat, U. b. Waheed, G. Karniadakis, En-deeponet: An enrichment approach for enhancing the expressivity of neural operators with applications to seismology, *Computer Methods in Applied Mechanics and Engineering* 420 (2024) 116681.
- [23] K. Kobayashi, J. Daniell, S. B. Alam, Improved generalization with deep neural operators for engineering systems: Path towards digital twin, *Engineering Applications of Artificial Intelligence* 131 (2024) 107844.
- [24] I. Sahin, C. Moya, A. Mollaali, G. Lin, G. Paniagua, Deep operator learning-based surrogate models with uncertainty quantification for optimizing internal cooling channel rib profiles, *International Journal of Heat and Mass Transfer* 219 (2024) 124813.
- [25] S. Koric, D. W. Abueidda, Data-driven and physics-informed deep learning operators for solution of heat conduction equation with parametric heat source, *International Journal of Heat and Mass Transfer* 203 (2023) 123809.
- [26] R. B. Hossain, F. Ahmed, K. Kobayashi, S. Koric, D. Abueidda, S. B. Alam, Virtual sensing-enabled digital twin framework for real-time monitoring of nuclear systems leveraging deep neural operators, *npj Materials Degradation* 9 (2025) 21.
- [27] J. He, S. Kushwaha, J. Park, S. Koric, D. Abueidda, I. Jasiuk, Sequential deep operator networks (s-deeponet) for predicting full-field solutions under time-dependent loads, *Engineering Applications of Artificial Intelligence* 127 (2024) 107258.
- [28] A. Vaswani, N. Shazeer, N. Parmar, J. Uszkoreit, L. Jones, A. N. Gomez, L. u. Kaiser, I. Polosukhin, Attention is all you need, in: I. Guyon, U. V. Luxburg, S. Bengio, H. Wallach, R. Fergus, S. Vishwanathan, R. Garnett (Eds.), *Advances in Neural Information Processing Systems*,

volume 30, Curran Associates, Inc., 2017.

- [29] S. Cao, Choose a transformer: Fourier or galerkin, *Advances in neural information processing systems* 34 (2021) 24924–24940.
- [30] X. Liu, B. Xu, L. Zhang, Ht-net: Hierarchical transformer based operator learning model for multiscale pdes (2022).
- [31] Z. Li, K. Meidani, A. B. Farimani, Transformer for partial differential equations' operator learning, *arXiv preprint arXiv:2205.13671* (2022). doi:10.48550/arXiv.2205.13671.
- [32] Z. Hao, Z. Wang, H. Su, C. Ying, Y. Dong, S. Liu, Z. Cheng, J. Song, J. Zhu, Gnot: A general neural operator transformer for operator learning, in: *International Conference on Machine Learning*, PMLR, 2023, pp. 12556–12569.
- [33] Q. Liu, V. Zhong, H. Meidani, D. Abueidda, S. Koric, P. Geubelle, Geometry-informed neural operator transformer, *arXiv preprint arXiv:2504.19452* (2025). doi:doi.org/10.48550/arXiv.2504.19452.
- [34] B. Shih, A. Peyvan, Z. Zhang, G. E. Karniadakis, Transformers as neural operators for solutions of differential equations with finite regularity, *Computer Methods in Applied Mechanics and Engineering* 434 (2025) 117560. doi:10.1016/j.cma.2024.117560.
- [35] S. Kushwaha, J. Park, S. Koric, J. He, I. Jasiuk, D. Abueidda, Advanced deep operator networks to predict multiphysics solution fields in materials processing and additive manufacturing, *Additive Manufacturing* (2024) 104266.
- [36] B. Mildenhall, P. P. Srinivasan, M. Tancik, J. T. Barron, R. Ramamoorthi, R. Ng, Nerf: Representing scenes as neural radiance fields for view synthesis, *Communications of the ACM* 65 (2021) 99–106. doi:10.48550/arXiv.2003.08934.
- [37] P. Kozłowski, B. Thomas, J. Azzi, H. Wang, Simple constitutive equations for steel at high temperature, *Metallurgical and Materials Transactions A* 23 (1992) 903–918.
- [38] H. Zhu, Coupled Thermo-Mechanical Finite-Element Model with Application to Initial Solidification, Ph.D. thesis, University of Illinois at Urbana-Champaign, Urbana, IL, USA, 1996.
- [39] Dassault Systèmes Simulia Corp., *Abaqus/Standard User's Manual*, Version 2022, Johnston, RI, USA, 2022.
- [40] S. Koric, B. G. Thomas, Efficient thermo-mechanical model for solidification processes, *International Journal for Numerical Methods in Engineering* 66 (2006) 1955–1989.
- [41] M. Zappulla, S. Cho, S. Koric, H. Lee, S. Kim, B. Thomas, Multiphysics modeling of continuous casting of stainless steel, *Journal of Materials Processing Technology* 278 (2020) 116469.
- [42] D. W. Abueidda, S. Koric, N. A. Sobh, H. Sehitoglu, Deep learning for plasticity and thermo-viscoplasticity, *International Journal of Plasticity* 136 (2021) 102852.
- [43] NCSA, Delta user documentation, 2025. <https://docs.ncsa.illinois.edu/systems/delta/en/latest/index.html>.
- [44] NCSA, Delta ai user documentation, 2025. <https://docs.ncsa.illinois.edu/systems/deltaai/en/latest/index.html>.